Identification of the representative crack length evolution in a multi-level interface model for quasi-brittle masonry

A. Rekik[1], F. Lebon[2]

[1] *Institut PRISME, Polytech'Orléans,* 8 *rue Léonard de Vinci,* 45072 *Orléans Cedex* 2
[2] *LMA CNRS UPR* 7051*, Université de Provence,* 13*, Chemin Joseph Aiguier,* 13402 *Marseille Cedex* 20

Abstract

It is proposed here to identify the law of crack length evolution with a small number of parameters governing a recently presented model [13] describing the interface behaviour in damaged masonry. Studies on non-confined medium- and large-sized masonry structures have shown that it is necessary to obtain a linear increasing crack in the post-peak part of the "stress-strain or displacement" diagram. In confined masonry structures showing softening and sliding parts, the results obtained with this crack evolution failed to match the experimental data. The crack lengths identified in the post-peak part at several points on the experimental "stress-displacement" diagram show that the representative crack length is a bi-linear or trilinear function describing the increase in the crack length with respect to the decrease in the shear stress. Numerical studies on medium- and large-sized masonry structures consisting of the same materials subjected to various loads were performed to determine the ultimate crack length, and the results are relatively insensitive to the size of the masonry and the type of the load applied. The numerical local fields determined in the elementary and full-scale structures investigated were used to test the validity of the present model at the local scale, as well as to obtain an additional unilateral condition in the case of compressed masonry structures in order to prevent overlapping between the masonry components.

Key words: masonry, laminate, homogenization, law of crack evolution, asymptotic analysis, interface, identification, unilateral contact

1. Introduction

Interface models for assessing the safety of civil and historical masonry constructions have attracted considerable attention, since their resistance depends to a large extent on the brick/mortar interfacial properties. In fact, mortar joints are usually less strong than masonry units, which explains the existence of planes of weakness along which cracks can propagate. Several models have been developed and presented in the literature for studying and predicting the behavior of masonry structures. Depending on the level of accuracy and simplicity required, either macro- or micro-modeling strategies can be used for this purpose.

In continuum structural and macro-models, bricks, mortar and brick-mortar interfaces are smoothed out into a homogeneous continuum, the average properties of which are identified at the level of the constituents, taking their geometric arrangement into account. This approach is applicable when the dimensions of a structure are sufficiently large for the ratio between the average stresses and average strains to be acceptable such as the macro-models (classical no-tension models [1, 2, 3]) have been widely developed in the past. During the last few decades, several attempts have been made to assess the average properties of masonry panels. The models developed for this purspose include micropolar Cosserat continuum models [4, 5] as well as applications of the mathematical theories of homogenization to periodic [6, 7] and non-periodic media. To describe the inelastic behaviour of structural masonry, some authors have combined homogenization techniques with a continuum damage mechanics approach [8, 15, 16]. Other authors such as Alpa and Monetto [19] and de Buhan and de Felice [17], have defined suitably macroscopic yield failure surfaces. Other applications of homogenization theory to estimating the conditions at failure as well as the macroscopic properties include those presented by Luciano and Sacco [18] and Cluni and Gusella [20]: the former authors dealt with periodic microstructures, whereas the latter focused on non-periodic masonry-work. Macro-approaches obviously require a preliminary mechanical characterization of the model, based on experimental laboratory or in situ tests [33, 34].

In studies based on micro analysis, two main approaches have been used: the simplified approach, which is the more refined, and the detailed micro-modeling approach.

Simplified methods consist in modeling the bricks, mortar and interface separately by adopting suitable constitutive laws for each component. This ap-

proach gives highly accurate results, especially at local level, since it involves specifying the exact joint positions and adopting appropriate constitutive models for the blocks, mortar and interfaces.
A simplified micro-model is an intermediate approach, where the properties of the mortar and the mortar interface unit are lumped into a common element, while expanded elements are used to model the brick units. Although this model reduces the computational cost of the analysis, some accuracy is obviously lost.
Several authors [21, 22, 23, 24] have established that the interface elements reflect the main interactions occuring between bricks and mortar. Several methods have been presented for modeling the behavior of interfaces with zero thickness and predicting their failure modes. Giambanco et al. [10], for examples expressed the constitutive law at the interface in terms of contact traction and the relative displacements of the two surfaces interacting at the joint. The fracture of the joint and the subsequent sliding are associated with the interface yield condition, which contains internal variables describing the joint evolution and induces hardening and softening behavior, usually accompanied by dilatancy. Method based on limit analysis combined with a homogenization technique was recently shown to be a powerful structural analysis tool, giving accurate collapse predictions: de Buhan and de Felice [17], for example, have presented a homogenized model of this kind which can be used for the limit analysis of masonry walls. The units are assumed in this model to be infinitely resistant and the joints are taken to be interfaces with zero thickness having a friction failure surface. In addition, the brittle damage model developed in [18, 23] involves an elementary cell composed of units, mortar and a finite number of fractures at the interfaces.
This work aims to identify the crack length evolution laws governing a recently proposed constitutive equation [13] with small number parameters for micro-cracked interfaces of masonry structures. It objects also to study the effect of the masonry structure size and of the load type on these identified parameters. Experimental tests [34, 35] on small and large masonry panels have been used to estimate the small number of parameters describing the micro-crack evolution law and leading to the best fit between the numerical and experimental tests. Moreover, this paper study the effect of the load type and the masonry structure size on the estimated nonlinear micro-crack evolution law governing the interface constitutive equation. In the case of a masonry structure under a compression load, the evaluation of the local numerical fields incites us to add a unilateral contact condition in order to

ovoid the overlap between the bricks and the joints constituents.
This paper is organized as follows: in section 2, the principles underlying the previously presented constitutive equation for micro-cracked masonry interfaces is briefly described. Section 3 describes with numerical studies on non-confined masonries panels at various sizes, which a linearly increasing crack length evolution gives a satisfactory fit with the experimental diagrams. At the end of this section, we identify the interface stiffnesses after adopting an additional unilateral condition in order to prevent overlapping between masonry components subjected to compression loads. Section 4 deals with the case of medium-sized confined masonry panels tested under shear loading conditions and subjected to various confining pressures. These structures undergo softening and sliding processes after the peak in the load. To fit the experimental results, the identification performed at several points on the experimental diagrams showed that the effective crack length must obey at least a bilinear function after the peak in the load.

2. A brief outline of the model

Masonry units have generally been discretized using continuum elements, whereas joints have been modeled in the form of weakness planes, using interface elements. The main limitation of this approach is the fact that it is not suitable for describing the interactions between joints and brick units. The most original feature of the model proposed here is that it includes a third material inserted between the units and mortar, which accounts for the noticeable differences generally existing between the mechanical properties of bricks and mortar, which were classically assumed to be isotropic. The properties of this third material are obtained by performing an exact linear homogenization procedure on a brick/mortar lamina (with the same volume fraction). This newly defined homogeneous material is then assumed to accurately account for the mechanical interactions between mortar joints and brick units. In a second step, assuming the existence of micro-cracks with a parallel pattern of distribution, forming an angle ϕ with the e_1 direction (see Fig. (2)) in the newly defined homogeneous material, the effective properties of the damaged material are determined using a micro-mechanical model available in the literature. As explained above, the 3-D material is located between brick units and mortar joints; its thickness must therefore be zero. For this purpose, asymptotic limit analysis is performed to shift from the 3-D to 2-D framework and thus express the normal and tangential stiffness of the

brick/mortar interface thus defined. The local fields of a three-phase loaded masonry structure are then simulated using the CAST3M FE code [51]. Further details about the steps required to model the brick-mortar interface will be given below.

2.1. Effective properties of the brick-mortar lamina

Non-reinforced masonry is a heterogeneous material consisting classically of a regular or irregular arrangement of brick units. The mortar binding the brick units together is classically taken to constitute the plane of weakness of the masonry structure. Due to the fact that damage occurs mostly at the interface between brick and mortar materials, we assume the existence of an extremely thin layer of material between each brick unit and its mortar joint. The mechanical properties of this layer are obtained by applying an asymptotic limit analysis procedure [41, 42, 43, 47]. For this purpose, it is proposed first to obtain the mechanical properties of the 3-D material obtained by homogenizing those of brick and mortar. Assuming brick and mortar to be isotropic and linear elastic materials, the homogenization of the brick/mortar lamina can be carried out exactly using an analytical homogenization formulation, as described in [13]. The homogeneous equivalent undamaged material, denoted hereafter by HEM^u, is transversally isotropic and characterized by the effective compliance tensor $\tilde{S}^u$ written in the form (1) with respect to the classical Voigt notation. In what follows, exponents h and v correspond to bed and head joints, respectively. e_3 and e_1, represent the HEM^{uh} and HEM^{uv} revolution axis, respectively, as shown in figure (1).

[Figure 1 about here.]

$$\tilde{S}^{uh} = \begin{pmatrix} \frac{1}{\tilde{E}_1^0} & -\frac{\tilde{\nu}_{12}^0}{\tilde{E}_1^0} & -\frac{\tilde{\nu}_{13}^0}{\tilde{E}_1^0} & 0 & 0 & 0 \\ -\frac{\tilde{\nu}_{12}^0}{\tilde{E}_1^0} & \frac{1}{\tilde{E}_1^0} & -\frac{\tilde{\nu}_{13}^0}{\tilde{E}_1^0} & 0 & 0 & 0 \\ -\frac{\tilde{\nu}_{13}^0}{\tilde{E}_1^0} & -\frac{\tilde{\nu}_{13}^0}{\tilde{E}_1^0} & \frac{1}{\tilde{E}_3^0} & 0 & 0 & 0 \\ 0 & 0 & 0 & \frac{1}{\tilde{G}_{23}^0} & 0 & 0 \\ 0 & 0 & 0 & 0 & \frac{1}{\tilde{G}_{23}^0} & 0 \\ 0 & 0 & 0 & 0 & 0 & \frac{1}{\tilde{G}_{12}^0} \end{pmatrix} \tag{1}$$

For further details about the method of obtaining the $\tilde{S}^{uh}$ components, see [13].

2.2. Effective properties of the micro-cracked material HEM^c

In the previous step, in the case of bed joints, an uncracked homogeneous material HEM^{uh} was defined, based on the known properties of brick and mortar. Now assuming the presence of parallel micro-cracks to the e_1 axis in this material, it is necessary to determine its effective properties. Many studies have dealt with assessing the effective elastic properties of damaged materials with defects of various kinds (holes and/or cracks). The choice of modeling method depends here mainly on the interactions between cracks. The earliest studies focused on sparsely distributed cracks and on the interactions between them. The most widely used models of this kind are those based on the self-consistent (SC) method [26, 27] and the Mori-Tanaka (MT) method [28]. When the cracks are closely spaced, i.e., crack densities are higher, the interactions cannot be ignored. Determining the effective properties is significantly more complex in this case. Several approaches can be used here, depending on the kind of interactions to be modeled. In the pioneering study by Kachanov et al. [36] on these lines, the behaviour of a material including arbitrarily distributed holes with various aspect ratios was described. Other authors have developed schemes accounting approximately for the interactions between the matrix and the defect as well as the effects of cracks between them, such as the differential scheme [30, 31], the SC model [29] and the Ponte-Castañeda and Willis (PCW) homogenization

scheme [32].
For the sake of simplicity, we started to model the degradation of the brick-mortar interface taking only the interactions between micro-cracks into account and neglecting the interactions with the matrix of the HEM^u material. Problems involving penny-shaped cracks and 3-D shapes are generally complex and must be solved in a 3-D setting. In this paper, for the sake of simplicity, we assume the existence of a small number of rectilinear cracks $2l^{(k)}$ in length. To solve this 2-D problem it is proposed to apply the method proposed by Kachanov et al. [36] to determine the equivalent properties of the damaged HEM^u material. The accuracy of this model, which generally depends on the density of the cracks, is satisfactory up to quite small distances between cracks (distances much smaller than the crack width).
Rectilinear cracks are assumed to be located on the plane (e_1, e_3) in a representative area $A = L_0 e$, where L_0 is the brick length and e is the thickness of the micro-cracked HEM^u material. In the case of the present 2-D problem, the Kachanov model includes a global parameter called the crack density, which is defined by the number and the length of all the cracks given by $\rho = \frac{1}{A}\sum_k \left(l^{(k)}\right)^2$.

[Figure 2 about here.]

The main result obtained with the Kachanov model is that the average value of the crack opening displacement (COD) vector "b" is colinear with the average stress $\bar{\sigma}$ as follows:

$$< b >= n.\bar{\sigma}.B$$

where n is a vector normal to the crack. The components of the symmetric B second order tensor depend on those of the uncracked homogeneous HEM^u material, i.e. on the components of $\tilde{S}^u$ and on the orientation of the crack with respect to the matrix anisotropy

[Figure 3 about here.]

$$\begin{cases} B_{tt} = C(1 - Dcos2\phi)l \\ B_{nn} = C(1 + Dcos2\phi)l \\ B_{tn} = CD(sin2\phi)l \end{cases} \quad (2)$$

where l is the length of the half representative rectilinear micro-crack in the HEM^u material, as shown in Fig. (2). We recall that ϕ is the angle between

the vector t tangential to the crack and the principal axis e_1, as illustrated in figure (3). C and D are scalars which are independent of the representative micro-crack half length parameter l, and are given by

$$\begin{cases} C^h = \dfrac{\pi}{4}\dfrac{\sqrt{\tilde{E}_1^{uh}}+\sqrt{\tilde{E}_3^{uh}}}{\sqrt{\tilde{E}_1^{uh}\tilde{E}_3^{uh}}}\left(\dfrac{1}{\tilde{G}_{13}^{uh}}-2\dfrac{\tilde{\nu}_{13}^{uh}}{\tilde{E}_1^{uh}}+\dfrac{2}{\sqrt{\tilde{E}_1^{uh}\tilde{E}_3^{uh}}}\right)^{\frac{1}{2}} \\ D^h = \dfrac{\sqrt{\tilde{E}_1^{uh}}-\sqrt{\tilde{E}_3^{uh}}}{\sqrt{\tilde{E}_1^{uh}}+\sqrt{\tilde{E}_3^{uh}}} \end{cases} \tag{3}$$

$\tilde{E}_1^{uh}$, $\tilde{E}_3^{uh}$, $\tilde{\nu}_{13}^{uh}$ and $\tilde{G}_{13}^{uh}$ are the elastic engineering constants of the crack-free HEM^{uh} material. On the principal axes, the effective engineering moduli of HEM^c denoting the homogeneous material equivalent to the damaged HEM^u are given by

$$\begin{cases} \dfrac{\tilde{E}_1^c}{\tilde{E}_1^u} = \dfrac{1}{1+2\rho sin^2\phi(B_{tt}cos^2\phi+B_{nn}sin^2\phi-B_{nt}sin2\phi)\tilde{E}_1^u} \\ \dfrac{\tilde{E}_3^c}{\tilde{E}_3^u} = \dfrac{1}{1+2\rho cos^2\phi(B_{tt}sin^2\phi+B_{nn}cos^2\phi+B_{nt}sin2\phi)\tilde{E}_3^u} \\ \dfrac{\tilde{G}_{13}^c}{\tilde{G}_{13}^u} = \dfrac{1}{1+\rho(B_{nn}sin^22\phi+B_{tt}cos^22\phi-B_{nt}sin4\phi)\tilde{G}_{13}^u} \\ \dfrac{\tilde{\nu}_{13}^c}{\tilde{E}_1^c} = \dfrac{\tilde{\nu}_{13}^u}{\tilde{E}_1^u} \end{cases} \tag{4}$$

In the bed masonry joints, the cracks are assumed to run parallel to the principal axis e_1, i.e. with the crack orientation $\phi = 0$. Under plane stress conditions, the components of the compliance tensor $\tilde{S}^c$ in the (e_1, e_3) plane read

$$\tilde{S}^{ch} = \tilde{S}^c(0) = \begin{pmatrix} \dfrac{1}{\tilde{E}_1^{uh}} & -\dfrac{\tilde{\nu}_{13}^{uh}}{\tilde{E}_1^{uh}} & 0 \\ -\dfrac{\tilde{\nu}_{13}^{uh}}{\tilde{E}_1^{uh}} & (\dfrac{1}{\tilde{E}_3^{uh}}+2\rho B_{nn}(0)) & 0 \\ 0 & 0 & (\dfrac{1}{\tilde{G}_{13}^{uh}}+\rho B_{tt}(0)) \end{pmatrix} \tag{5}$$

where

$$\begin{cases} B_{tt}(0) = C^h(1 - D^h)l \\ B_{nn}(0) = C^h(1 + D^h)l \\ B_{tn}(0) = 0 \end{cases} \tag{6}$$

As shown in relations (5), the effective properties of the cracked lamina are sensitive to the effective properties of the uncracked lamina HEM^{uh} and to the representative crack length. Inverting the compliance tensor $\tilde{S}^{ch}$ gives the corresponding stiffness tensor $\tilde{C}^{ch}$ associated with the properties of HEM^{ch}.

2.3. Interface constitutive law

It has been assumed that cracks exist only in the plane (e_1, e_3) parallel to either the principal axis e_1 (in the case of bed joints) or to the e_3 vector (in the case of head joints). We have therefore focused only on the pair of components ($\tilde{C}^{ch}_{3333}$, $\tilde{C}^{ch}_{3131}$) and ($\tilde{C}^{cv}_{1111}$, $\tilde{C}^{cv}_{1313}$) corresponding to the bed and head interface stiffness, respectively. Now focusing on the head interface stiffnesses, the inversion of the compliance tensor $\tilde{S}^{ch}$ leads to expressing the components ($\tilde{C}^{ch}_{3333}$, $\tilde{C}^{ch}_{3131}$) as a function of the micro-crack density parameter ρ, and the angle ϕ is null.

$$\begin{aligned} \tilde{C}^{ch}_{3333} &= \frac{\alpha^h_{33} + \beta^h_{33}\rho}{\alpha^{0h}_{33} + \beta^{0h}_{33}\rho + \gamma^{0h}_{33}\rho^2} \\ \tilde{C}^{ch}_{3131} &= \frac{1}{2}\frac{\alpha^h_{13} + \beta^h_{13}\rho}{\alpha^{0h}_{13} + \beta^{0h}_{13}\rho + \gamma^{0h}_{13}\rho^2} \end{aligned} \tag{7}$$

α^h_{ij}, β^h_{ij}, α^{0h}_{ij}, β^{0h}_{ij} and γ^{0h}_{ij} are scalars which are independent of the crack density parameter ρ. As established in [13], the normal and tangential stiffness of the bed interfaces are determined as follows:

$$\begin{aligned} C^h_N &= \frac{\tilde{C}^{ch}_{3333}}{e}(e \to 0) \\ C^h_T &= \frac{\tilde{C}^{ch}_{3131}}{e}(e \to 0) \end{aligned} \tag{8}$$

Replacing ρ by the term $\dfrac{l^2}{eL^h_0}$ in expressions (7), we obtain

$$\begin{aligned} C^h_N &= \frac{\beta^h_{33}L^h_0}{\gamma^{0h}_{33}l^2} = \frac{L^h_0}{2B_{nn}(0)l^2} \\ C^h_T &= \frac{\beta_{13}L^h_0}{\gamma^0_{13}l^2} = \frac{L^h_0}{4B_{tt}(0)l^2} \end{aligned} \tag{9}$$

As the components B_{nn} and B_{tt} depend on the half crack length l (see relation (2), the expressions for the interface stiffness C_N and C_T at the bed position read as follows:

$$\begin{aligned} C_N^h &= \frac{L_0^h}{2C(1+D)l^3} \\ C_T^h &= \frac{L_0^h}{4C(1-D)l^3} \end{aligned} \tag{10}$$

It is worth noting that the properties of the material HEM^{cv}, which is transversally isotropic with e_1 as the revolution axis, are deduced from those of the material HEM^{ch} by making a simple 90-degree rotation. Therefore, the normal and tangential stiffness of the head joints read:

$$\begin{aligned} C_N^v &= \frac{\tilde{C}_{1111}^{cv}}{e}(e \to 0) = \frac{L_0^v}{L_0^h}\, C_N^h \\ C_T^v &= \frac{\tilde{C}_{1313}^{cv}}{e}(e \to 0) = \frac{L_0^v}{L_0^h}\, C_T^h \end{aligned} \tag{11}$$

These defined stiffnesses can be clearly seen to decrease as the applied load F (stress τ), increases up to failure. In addition, they are closely related to the law of micro-crack evolution $l = f(F \text{ or } \tau)$ which will be identified in the case of masonry structures of various sizes under loads of various kinds in the following section. The crack length evolution is assumed to show a similar tendency at the head and bed interfaces.

3. Estimation of the representative law of micro-crack evolution based on experimental tests

In view of expressions (10), one of the most important steps consists in defining, testing and validating a law governing the crack length evolution. An alternative solution consists in defining directly by choosing crack lengths at several points on experimental diagrams. Hereafter, it is necessary to distinguish between the case of quasi-brittle failures, with which the "stress-strain" diagram shows a "plateau" in the post-peak load part and those showing a softening and sliding parts after the peak in the load. In fact, numerical tests carried out on non-confined and confined masonry panels have shown that the laws of crack length evolution available so far in the case of non-confined masonry are not able to reproduce the softening and sliding parts seen in the case of the confined masonries.

3.1. Simulation of non-confined loaded masonry panels of various sizes

In order to model as accurately as possible the "load-displacement" response of a quasi-brittle non-confined masonry structure subjected to a shear load (in the case of a seven brick panel (Fig. (16))) or a diagonal compression load (in the case of a wall (Fig. (11)), it is assumed that under the maximum load (or stress), denoted F^c (or τ_c), the representative micro-crack is inactive (i.e., its length remains constant and equal to the critical length l_c) and that it propagates from the maximum load up to the failure of the interface i.e. up to the ultimate load F^u or stress τ^u (as seen in Fig. (4)) reached at the ultimate crack length l_u. The values of the load parameters F^c and F^u (or stresses τ^c and τ^u) are determined from the experimental "load-displacement" curves [33, 34, 35]. The values of the lengths l_c and l_u are chosen so that the numerical global response matches the experimental "stress-strain" (or "stress-displacement") diagram satisfactorily. Figure (4) gives the evolution of the representative half crack length predicted, based on experimental data available in [13] on elementary walls consisting of triplet bricks, seven bricks (figure (8)) and a large wall as shown in figure (13), as described in the following sections.

[Figure 4 about here.]

[Figure 5 about here.]

In order to test the validity of the law of crack length evolution described in Fig. (4) and to identify the parameters involved (F^c, F^u, l_c and l_u), the experimental data obtained by Gabor et al. [33] on elementary masonry walls consisting of 7 bricks under shear loading and on a wall subjected to diagonal compression were used. The geometry and boundary conditions are given in Fig. (16) (without the confining pressure σ) and Fig. (11) in the case of 7 bricks and the wall, respectively. Table (1) lists the mechanical properties of the bricks and mortar constituting the prism and the wall [34]. Because of the symmetry of the prism problem, only half-structures will be used in the computations.

[Table 1 about here.]

3.1.1. Simulation of a non-confined medium-sized masonry panel under shear loading

The masonry specimen studied in this part consists of seven hollow bricks subjected to a shear load without any confining pressure. To calculate the global and local mechanical fields, it is necessary to determine the characteristics and the parameters of bed interfaces, 50 mm in length, denoted by h. The stiffness of head interfaces, 210 mm and 100 mm in length, denoted by v^1 and v^2, respectively, is deduced from that of h, using the following relations:

$$C_N^{v1} = (210/50)\, C_N^h \quad \text{and} \quad C_T^{v1} = (210/50)\, C_T^h$$
$$C_N^{v2} = (100/50)\, C_N^h \quad \text{and} \quad C_T^{v2} = (100/50)\, C_T^h$$

[Figure 6 about here.]

[Figure 7 about here.]

[Figure 8 about here.]

In the case of bed interfaces, the compliance tensor $\tilde{S}^{uh}$ of the effective undamaged material HEM^{uh} reads

$$\tilde{S}^{uh} = 10^{-4} \begin{pmatrix} 1.190 & -0.357 & -0.357 & 0 & 0 & 0 \\ -0.357 & 1.190 & -0.357 & 0 & 0 & 0 \\ -0.357 & -0.357 & 1.525 & 0 & 0 & 0 \\ 0 & 0 & 0 & 4.265 & 0 & 0 \\ 0 & 0 & 0 & 0 & 4.265 & 0 \\ 0 & 0 & 0 & 0 & 0 & 3.095 \end{pmatrix} \tag{12}$$

The associated engineering constants are:

$$\tilde{E}_1^{uh} = \tilde{E}_2^{uh} = 8400\,\text{MPa},\ \tilde{G}_{12}^{uh} = 3230.7\,\text{MPa}, \tilde{\nu}_{12}^{uh} = 0.3,$$
$$\tilde{E}_3^{uh} = 6557.93\,\text{MPa},\ \tilde{G}_{13}^{uh} = 2344.32\,\text{MPa and}\ \tilde{\nu}_{13}^{uh} = 0.3$$

The constants C and D (3) used to evaluate the components of the COD tensor $B(0)$ are:

$$C = 0.000456 \quad \text{and} \quad D = 0.061810 \tag{13}$$

The normal and tangential stiffness of the bed interfaces are then given by the following expressions:

$$C_N^h = 51570.5/l^3\ (N/mm^2) \quad \text{and} \quad C_T^h = 29182.9/l^3\ (N/mm^2)$$

At head interfaces $v1$ and v^2, these expressions are:

$$\begin{array}{l} C_N^{v1} = 216596/l^3(N/mm^2) \quad \text{and} \quad C_T^{v1} = 122568/l^3(N/mm^2) \\ C_N^{v2} = 103141/l^3(N/mm^2) \quad \text{and} \quad C_T^{v2} = 58365.8/l^3\ (N/mm^2) \end{array} \tag{14}$$

The mesh for the half in-plane structure of this specimen consists of 4872 Q4 finite elements. Similar loading and boundary conditions (see Figure (6) with no confinement pressure σ) to those used by Gabor et al [33] were adopted here.

[Figure 9 about here.]

The predictions of the model for an elementary masonry panel based on the crack length law shown in Figure (4) with the identified crack parameters $l_u = 1.3\ \mu m$ and $l_c = 1.51\ \mu m$ at the critical and ultimate stresses $\tau_c = 1.75\ MPa$ and $\tau_u = 1.9\ MPa$ identified on the basis of experimental data showed good agreement with the experimental results (see Figure (8)). In the case of this elementary masonry structure, it was concluded that failure will occur when the interface stiffnesses, per $mm.l$, reach the following values:

$$C_N = 3\,10^{11}(N/mm^3) \quad \text{and} \quad C_T = 1.74\,10^{11}(N/mm^3)$$

Figure (6) shows the final geometrical configuration of the prism when the crack length reaches its ultimate value l_u. In the case of local fields observed during the failure phase shown in Figure (9) confirm that this crack length law with the suitable parameters values can be used to accurately predict the localization of the shear stress concentration where failure occurs, as in the experimented specimen (see figure (20)).
The crack lengths identified at two supplementary points on the experimental prism as shown in figure (7) confirms that the crack length increased linearly in the post-peak part.

3.1.2. Case of a wall under diagonal compression without unilateral contact condition

The accuracy of the present model based on the crack length law (Fig. (4)) and suitable couplets of parameters (τ_c, l_c) and (τ_u, l_u) will be checked

below in the case of the masonry with large in-plane dimensions (870 mm x 830 mm) previously tested by Gabor et al. [33]. In this specimen, the head and bed interface lengths were 50 mm and 210 mm, respectively. In the examples described below, the material parameters of the bricks and mortar were identical to those of the medium-sized wall described in Table (1). The compliance tensor of horizontal uncracked brick/mortar lamina is given by expressions (12). The values of the associated constants C and D are given by (13). The normal and tangential stiffness of the bed and head interfaces are therefore identical to the stiffnesses h and $v1$ of the seven brick panel.
The identification of crack lengths at the critical and ultimate loads F_c and F_u yielded respectively to the values: $l_c = 1.6\,\mu m$ and $l_u = 1.61\mu m$. Good agreement was therefore obtained between the numerical and experimental data, as can be seen in Figure (12). Note that in this experimental test, $F_u = F_c = 251.77\,kN$, and the crack length evolution (Fig. (4)) therefore reduces to the function (Fig. (10)).
In the case of the wall, per $mm.l$, the interface stiffnesses at the failure phase is therefore given by the values:

$$C_N = 2.47\,10^{11}\,(N/mm^3) \quad \text{and} \quad C_T = 1.4\,10^{11}\,(N/mm^3)$$

Comparisons between the ultimate crack length identified for the wall and the non-confined masonry panels showed the existence of relative error of about 6.4%.

[Figure 10 about here.]

[Figure 11 about here.]

[Figure 12 about here.]

[Figure 13 about here.]

In what follows, bricks and mortar joints will be modeled using Q4 quadrangular finite elements. The following scaled deformed mesh (Figure (14)) was obtained for the ultimate diagonal strain with the ultimate half crack parameter: $l_c = 1.61\,\mu m$. This deformed configuration shows that the wall is not able to resist the diagonal compression, especially at the left top corner, where the load was applied. This is confirmed by the fact that the shear stresses are concentrated in this corner. Given suitable micro-crack lengths occurring during the failure phase, the present model can therefore be used to reproduce the local response of a large-sized loaded masonry specimen.

[Figure 14 about here.]

3.1.3. Effect of an additional unilateral contact condition on the interface stiffnesses

In order to avoid the overlaps which can be seen in Figure (14) to occur between the brick and mortar faces in the case of masonry structure subjected to compression loads, it is proposed to introduce unilateral contact conditions.
The relative displacement between two points located on the two surfaces in contact is denoted by $[u]$, where

$$[u] = u^b - u^m$$

and u^b (respectively u^m) is the displacement in the brick (respectively in the mortar). Let F be the density of the contact forces. We take n^b (respectively n^m) to denote the external unit normal vector to the boundary of the brick (respectively to the boundary of the mortar). The decomposition into normal and tangential parts is written

$$[u] = [u_n]n^b + u_t, \quad \text{with} \quad [u_n] = [u].n^b \tag{15}$$

$$F = F_n n^b + F_t, \quad \text{with} \quad F_n = F.n^b \tag{16}$$

Locally, the unilateral contact is given by the following relations

$$[u_n] \geq 0 \tag{17}$$

$$F_n - C_N[u_n] \geq 0 \tag{18}$$

$$(F_n - C_N[u_n])[u_n] = 0 \tag{19}$$

Relation (17) denotes the possibility that only decohesion will occur, and not penetration. Relation (18) expresses the fact that the normal stresses correspond only to compression. Relation (19) shows that at the brick/mortar interface, there are only two possibilities: contact or decohesion. This relation is commonly known as the complementary condition. This condition was imposed only for the 3 first ranges (from the 14^{th} to the 12^{th}) of bricks (at head and bed joints) where overlap has been observed.

[Figure 15 about here.]

The crack law parameters ensuring good agreement between the numerical and experimental "stress-strain" diagrams have the following values: $l_c =$

1.725 μm and $l_u = 1.728\ \mu m$ for $F_u = F_c = 251.77\ kN$. Per $mm.l$, the corresponding normal and tangential interfaces then read:

$$C_N = 2.\ 10^{11}\ (N/mm^3), \quad \text{and} \quad C_T = 1.13\ 10^{11}\ (N/mm^3)$$

When failure occurs, the additional unilateral contact condition therefore decreases the stiffnesses of the wall interfaces by about 21%.

3.2. Simulation of a confined medium-sized masonry panel under shear loading conditions

In the case of confined masonry panels subjected to shear loads with various confining stresses ($\sigma = 0.4$, 0.6, 0.8 and 1.2 MPa), the joint response differs from that observed under non-confined conditions, as shown in Figure (18). Experimental results are plotted in dashed lines. In the "stress-displacement" diagrams, the distinction will be made between three stresses: τ_c, τ_{cr} and τ_u, denoting the critical or maximum stress value, the end of the softening phase and the ultimate stress value in the sliding phase, respectively. Additional confining pressure was found to increase the cohesion between mortar and hollow bricks and thus to induce the occurrence of softening and sliding processes after the peak load has been reached. These softening and sliding parts cannot be modelled in the framework of a crack length evolution law similar to that used for a non-confined masonry panel (Figure (7)). In this case, a nonlinear piece-wise increasing representative crack length from the peak load up to failure gives better predictions. Numerical simulations on this structure adopting linear functions with a single slope describing the increase in the crack length and the decrease in the shear stress as described in Figure (5) and characterized only by two identified crack length parameters l_c and l_u at the maximum and ultimate stresses, respectively, show that the results obtained using crack length laws of this kind do not match the experimental "stress-displacement" diagrams. To obtain a better fit between the numerical and experimental data, the crack lengths were identified at several points on the experimental diagram. At various confining stresses, the changes in the crack lengths given, in figure (19), show that it is necessary to include a bilinear or trilinear function in the post-peak load part to account for the set of the softening and sliding parts. As shown in figure (19), these functions describe the increase in the crack length, while the shear stress decreases, in live with the properties of cohesive cracks [53, 54, 55]. In the identified functions $l = f(\tau)$ corresponding to confining stresses $\sigma = 0.8$ and $1.2\ MPa$, note the existence of a first

positive slope describing the increase in the crack length with the increase in the shear stress occurring before peak of load is reached. This first linear evolution of l is not included in the description of the crack length evolution in the softening and sliding parts given by the "stress-displacement" diagrams.

[Figure 16 about here.]

[Figure 17 about here.]

[Figure 18 about here.]

[Figure 19 about here.]

[Figure 20 about here.]

The numerical "stress-displacement" curves corresponding to the crack length functions depicted in Figure (19) are in line with experimental data as can be seen from Figure (18) with each of the confining stresses. Table(2) lists the ultimate crack lengths obtained at the various confining pressures tested. Note that the crack length l_u varies slightly with the confining pressure. Its main value is $l_u^{cp} = 1.61\,\mu m$. The relative errors e_r between l_u and the average value l_u^{cp} do not exceed 11%.

[Table 2 about here.]

Figure (17) gives the local shear stress distribution with a $0.4\,MPa$ confined small wall, which shows a local stress concentration at the longest vertical interface v^1, where the decohesion between brick and mortar mainly occurs, as in the experimentally tested specimen (Figure (20)).

3.3. Discussion of the results

Table (3) recapitulates the identified ultimate crack lengths giving a best fit between the numerical and experimental results at the failure of the wall with and without the unilateral contact condition. The relative difference between these values is taken to be negligible (about 7%). It was therefore proposed to calculate the mean ultimate crack length from the values available on wall interfaces at failure. The relative errors e_r between the identified crack lengths l_u and the mean value $l_u^w = 1.66$ obtained in the case of the wall were negligible (below 4%).

[Table 3 about here.]

Table (4) gives the identified (average) ultimate crack lengths obtained with masonry structures of various sizes under shear loads (with and without confining pressure) or diagonal compression loads (with and without the unilateral contact condition). Due to the negligible differences existing between these values, we will assume that failure occurs when the crack length reaches the average value of this set of identified crack lengths i.e. $l_u = 1.6\,\mu m$.

[Table 4 about here.]

In the case of masonry composed of constituents with the properties given in table (1), comparisons between the stiffnesses of the interfaces obtained with masonry of various sizes (see the e_r values for the stiffnesses) gave a mean stiffness value per $mm.l$, and upper and lower bounds for the properties thus identified:

$$\begin{cases} C_N^{av} = 252\,10^9 (N/mm^3) \quad \text{and} \quad C_T^{av} = 142.5\,10^9 (N/mm^3), \\ C_N^{av}(1 - 11\%) \leq C_N \leq C_N^{av}(1 + 17\%) \end{cases} \tag{20}$$

The discrepancies between the individual interface stiffnesses and the mean value obtained (maximum about 17%) can be explained by the fact that masonry mortar joints are man-made materials.

4. Conclusions

In this study, the identification of the crack length evolution law for masonry structures with various sizes subjected to shear and diagonal compression loads showed the ability of a recently presented model [13] to provide estimations for the stiffness of masonry interfaces. At failure, the discrepancies between the identified crack lengths were almost negligible (below 6%). The interface stiffnesses are inversely proportional to the cube of the ultimate crack length l_u which explains the maximum discrepancy of about 17%. An experimental campaign in which the joint mortar is consistently prepared and laid (constant thickness, regular rate of cover between brick and mortar) will help to reduce the discrepancies between the stiffnesses of interfaces at failure. To obtain a good fit between experimental and numerical data on loaded non-confined masonry structures in which the "stress-strain" diagrams show the occurrence of a "plateau" after the peak load (or stress), it

is necessary to adopt a linearly increasing crack length up to the failure, corresponding to the ultimate load applied. Number of parameters is reduced to 4 in this case: l_c, l_u, τ_c and τ_u. In the case of confined masonry structures under shear loading conditions, the present model gives good agreement with the experimental data, thanks to the introduction of a bilinear or trilinear function describing the increase in the crack length with the decrease in the shear stress in the post-peak part (softening and sliding parts). The number of parameters increases in this case to 6 or 8. In the post-peak part of the "stress-displacement" diagram, a single linear function describing the increase in the crack length with the decrease in the shear stress does not suffice to reproduce correctly the softening and sliding parts accurately.

References

[1] Marfia S., Sacco E., Numerical procedure for elasto-plastic no-tension model, International Journal of Computational Methods in Engineering Science and Mechanics, 6, 99-187 (2005).

[2] Lourenço P.B., Continuum model for masonry: parameter estimation and validation, ASCE Journal of Structural Engineering, 124(6), 642-652 (1998).

[3] Di Pasquale S., New trends in the analysis of masonry structures, Meccanica, 27, 173-84 (1992).

[4] Sulem J., Muhlhaus H.B., A continuum model for periodic two-dimensional block structures, Mechanics of Cohesive-Frictional Materials, 2, 31-46 (1997).

[5] Masiani R., Trovalusci P., Cauchy and Cosserat materials as continuum models of brick masonry, Meccanica, 31, 421-432 (1996).

[6] Anthoine A., Derivation of in-plane elastic characteristics of masonry through homogenization theory, International Journal of Solids and Structures, 32 (2), 137-163 (1995)

[7] Ushaksarei R., Pietruszczak S., Failure criterion for structural masonry based on critical plane approach, Journal of Engineering Mechanics ASCE 128 (7), 769-778 (2002).

[8] Zucchini A., Loureno P.B., A coupled homogenization-damage model for masonry cracking, Computers and Structures, 82, 917-929 (2004).

[9] Chaimoon K., Attard M., Modeling of unreinforced masonry walls under shear and compression, Engineering Structures 29, 2056-2068 (2007).

[10] Giambanco G., Di Gati L., A cohesive interface model for the structural mechanics of block masonry, Mechanica Research Communications, 24 (5), 503-512 (1997)

[11] Dobert C., Mahnken R., Stein E., Numerical simulation of interface debonding with a combined damage/friction constitutive model, Computational Mechanics, 25, 456-467 (2000).

[12] Kachanov M., Solids with cracks and non-spherical pores: proper parameters of defect density and effective elastic properties, International Journal of Fracture, 97, 1-32 (1999).

[13] Rekik A., Lebon F., Homogenization methods for interface modeling in damaged masonry, paper submitted to Computers and Structures in 2008

[14] Touzet M., Le Poulain, F., Aubert I., Puiggali M., The incremental self-consistent scheme applied to active stress corrosion cracks, Mechanics of Materials, 38, 620-632 (2006).

[15] Pegon P., Anthoine A., Numerical strategies for solving continuum damage problems with softening: application to the homogenization of masonry, Computers and Structures, 64, 623-642 (1997).

[16] Chengqing W., Hong H., Derivation of 3D masonry properties using numerical homogenization technique, International Journal For Numerical Methods in Engineering, 66, 1717-1737 (2006).

[17] de Buhan P., de Felice G., A homogenisation approach to the ultimate strength of brick masonry. Journal of the Mechanics and Physics of Solids, 45(7), 1085-104 (1997).

[18] Luciano R., Sacco E., Homogenisation technique and damage model for old masonry material, International Journal of Solids and Structures, 34(24), 3191-208 (1997).

[19] Alpa G., Monetto I., Microstructural model for dry block masonry walls with in-plane loading, 42(7), 1159-1175 (1994).

[20] Cluni F., Gusella V., Homogenisation of non-periodic masonry structures, International Journal of Solids ans Structures, 41, 1911-1923 (2004).

[21] Lotfi H.R., Shing P.B., Interface model applied to fracture of masonry structures, Journal of Structural Engineering ASCE 120(1), 63-80 (1994).

[22] Lourenço P.B., Rots J., A multi-surface interface model for the analysis of masonry structures, Journal of Engineering Mechanics ASCE 123(7), 660-668 (1997).

[23] Pelissou C., Lebon F., Asymptotic modeling of quasi-brittle interfaces, Computers and Structures, 87, 1216-1223 (2009).

[24] Pegon P., Pinto A., Géradin M., Numerical modeling of stone-block monumental structures, Computers and Structures, 79, 2165-2181 (2001).

[31] Hashin Z., The differential scheme and its application to cracked materials, Journal Mech Phys Solids, 36, 719-734 (1988).

[26] Budiansky B., O'Connell R.J., Elastic moduli of cracked solid, International Journal of Solids Struct., 12, 81-97 (1976).

[27] Hoenig A., Elastic moduli of a non-randomly cracked body, International Journal of Solids and Structures, 15, 137-154 (1979).

[28] Benveniste Y., On the Mori-Tanaka method in cracked solids, Mechanical Research Communications, 13, 193-201 (1986)

[29] Deng H., Nemat-Nasser S., Microcrack arrays in isotropic solids, Mechanics of Materials, 13, 15-36 (1992).

[30] Laws N., Dovrak G.J., The effect of fiber breaks and aligned penny-shaped cracks on the stiffness and energy release rates in unidirectional composites, International Journal of Solids and Structures, 23, 1269-1283 (1987).

[31] Hashin Z., The differential scheme and its application to cracked materials, Journal of the Mechanics and Physics of Solids, 36, 719-734 (1988).

[32] Ponte-Castañeda P., Willis J.R., The effect of spatial distribution on the behavior of composite materials and cracked media, Journal of the Mechanics and Physics of Solids, 43, 1919-1951 (1995).

[33] Gabor A., Ferrier E., Jacquelin E. and Hamelin P., Analysis of the inplane shear behaviour of FRP reinforced hollow brick masonry walls, Structural Engineering and Mechanics, 19, 237-260, (2005).

[34] Gabor A., Bennani A., Jacquelin E. and Lebon F., Modelling approaches of the in-plane shear behaviour of unreinforced and FRP strengthened masonry panels, Computers and Structures, 74, 277-288, 2006.

[35] Fouchal F., Lebon F., Titeux I., Contribution to the modelling of interfaces in masonry construction, Construction and Building Materials, 23, 2428-2441 (2009).

[36] Mauge C., Kachanov M., Effective elastic properties of an anisotropic material with arbitrarily oriented interacting cracks, Journal of the Mechanics and Physics of Solids, 42, 561-584 (1994).

[37] Kachanov M., Effective elastic properties of cracked solids: critical review of some basic concepts, Applied Mechanics Reviews, 45 (8), 304-335 (1992).

[38] Kachanov M., Elastic solids with many cracks and related problems, Advances in Applied Mechanics (ed. J. Hutchinson and T. Wu), 30, 259-445, Academic Press, New-York (1993).

[39] Chaboche J.L., Suquet P., Besson J., Endommagement et changement d'échelle, in: Bornert M., Bretheau T., Gilormini P. (Eds), Homogénéisation en mécanique des matériaux, tome2, Hermes Science, Chapter 3, 91-146 (2001).

[40] Lotfi H. R., Shing P. B., An appraisal of smeared crack models for masonry shear wall analysis, Computers and Structures 41, 413-425 (1991).

[41] Lebon F., Ronel-Idrissi S., First order numerical analysis of linear thin layers, ASME Journal of Applied Mechanics, 74, 824-828 (2007).

[42] Lebon F., Rizzoni R., Ronel-Idrissi S., Analysis of non-linear soft thin interfaces, Computers and Structures, 82, 1929-1938 (2004).

[43] Lebon F., Ould Khaoua A., Licht C., Numerical study of soft adhesively bounded joints in finite elasticity, Computational Mechanics, 21, 134-1998 (1998).

[44] Lebon F., Contact problems with friction: models and simulation, Simulation Modelling Practice and Theory, 11, 449-463 (2003).

[45] Rekik A., Bornert M., Auslender F., Zaoui A., A methodology for an accurate evaluation of the linearization procedures in nonlinear mean field homogenization, Comptes Rendus Mécanique, 333 (11), 789-795 (2005).

[46] Rekik A., Auslender F., Bornert M., Zaoui A., Objective evaluation of linearization procedures in nonlinear homogenization: A methodology and some implications on the accuracy of micromechanical schemes, International Journal of Solids and Structures, 44 (10), 3468-3496 (2007).

[47] Zaittouni F., Lebon F., Licht C., Étude théorique et numérique du comportement d'un assemblage de plaques, Comptes Rendus Mécanique, 330 (5), 359-364 (2002).

[48] Shao J.F., Hoxha D., Bart M., Homand F., Duveau G., Souley M., Hoteit N., Modeling of induced anisotropic damage in granites, International Journal of Rock Mechanics and Mining Sciences, 36, 1001-1012 (1999).

[49] Zaoui A., Propriétés non linéaires des composites: approches en champ moyen, in: Bornert M., Bretheau T., Gilormini P. (Eds), Homogénéisation en mécanique des matériaux, tome 2, Hermes Science, Chapter 1, 17-44 (2001).

[50] Bornert M., Suquet P., Propriétés non linéaires des composites: approches par les potentiels, in: Bornert M., Bretheau T., Gilormini P. (Eds), Homogénéisation en mécanique des matériaux, tome 2, Hermes Science, Chapter 2, 45-90 (2001).

[51] Cast3M official website: http://www-cast3m.cea.fr/cast3m/index.jsp

[52] Boutin C., Microstructural effects in elastic composites, International Journal of Solids and Structures, Vol. 33, pp. 1023-1051, 1996

[53] Park K., Paulino G. H., Roesler J. R., Determination of the kink point in the bilinear softenong model for concrete, Engineering Fracture Mechanics, 75, 3806-3818 (2008).

[54] Chaimoon K., Attard M. M., Experimental and numerical investigation of masonry under thee-point bending (in-plane), Engineering Structures, 31, 103-112 (2009)

[55] Parvanova S., Gospodiniv G., Development of "event-to-event" nonlinear technique to lightly reinforced concrete beams by simplified constitutive modeling, International Journal of Solids and Structures, In press

List of Figures

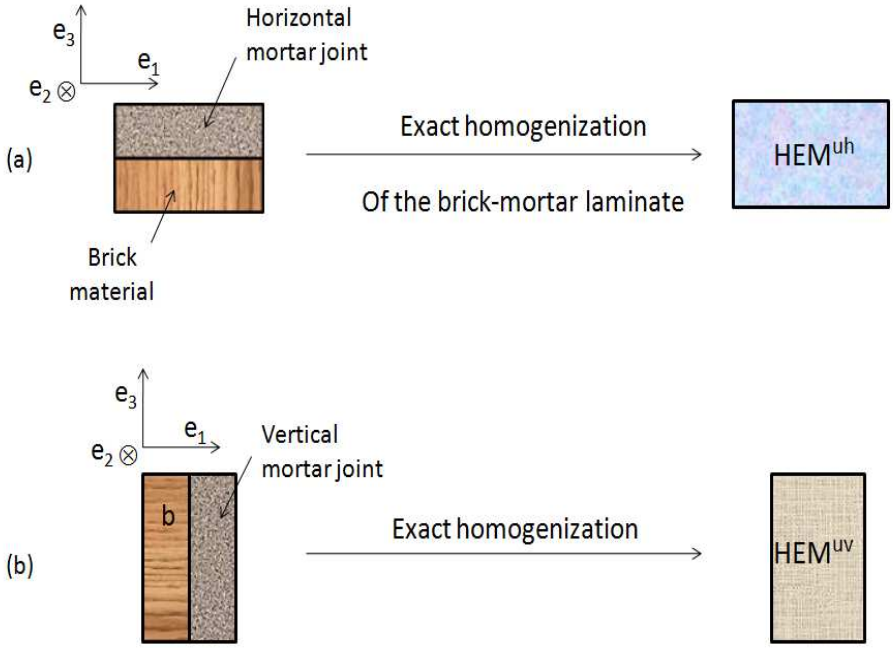

Figure 1: *Determination of the elastic properties of the third material (a brick/mortar lamina) located at bed (a) and head (b) joints.*

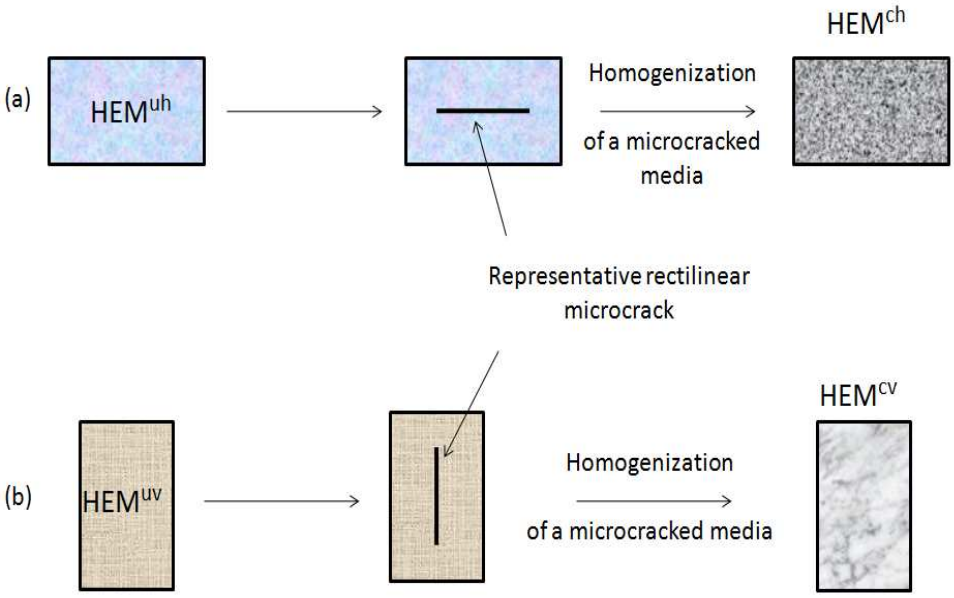

Figure 2: *Assessment of the effective properties of the micro-cracked bed (a) and head (b) joints using the Kachanov model.*

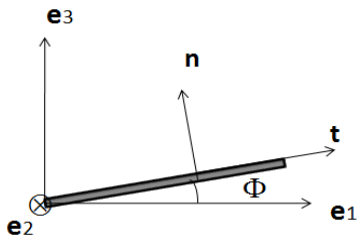

Figure 3: *Local crack vectors and the principal axis of the masonry.*

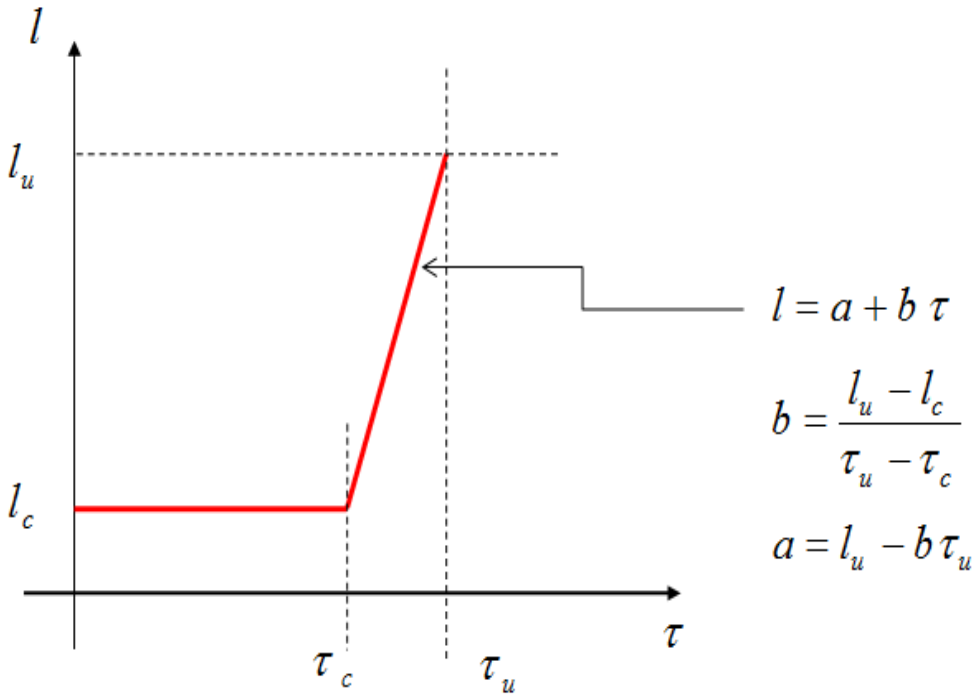

Figure 4: *A preliminary function describing the evolution of the crack half length with respect to the shear stress applied: the case of a triplet of hollow bricks [13], a non-confined seven brick structure and that of a wall.*

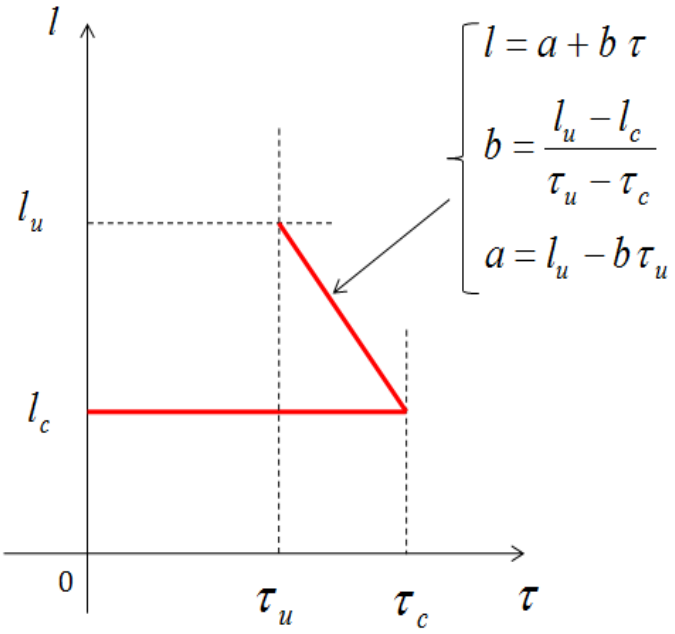

Figure 5: *A possible preliminary function describing the evolution of the crack half length with respect to the shear stress applied. The case of a small confined wall.*

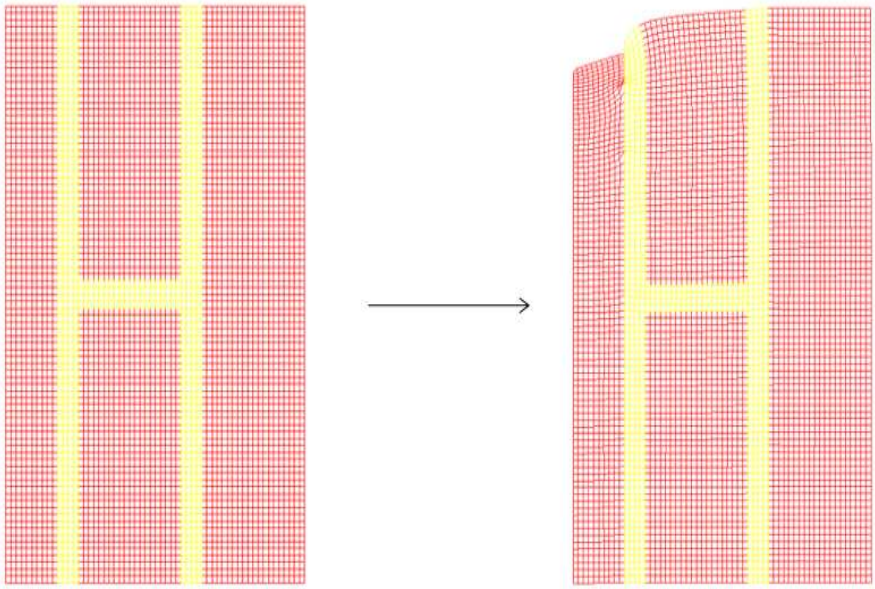

Figure 6: *Initial geometrical configuration and deformation of a small non-confined wall in a shear test at the identified ultimate crack length* $l_u = 1.51\mu m$

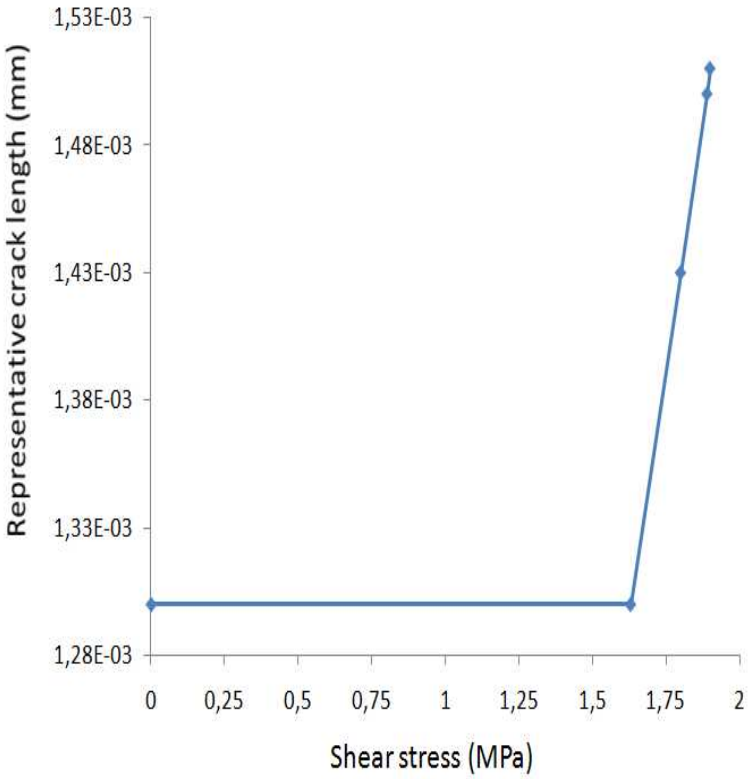

Figure 7: *Identified crack length law in the case of small non-confined wall under shear loading conditions*

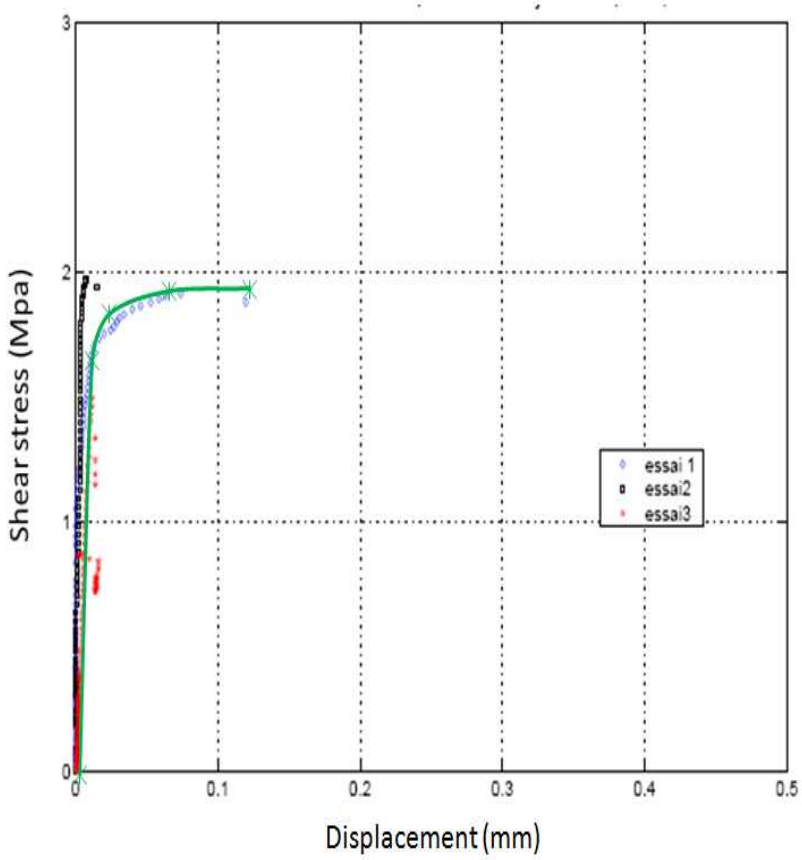

Figure 8: *Experimental and numerical response of the small non-confined wall under shear loading conditions based on the identified crack length law (fig. 7)*

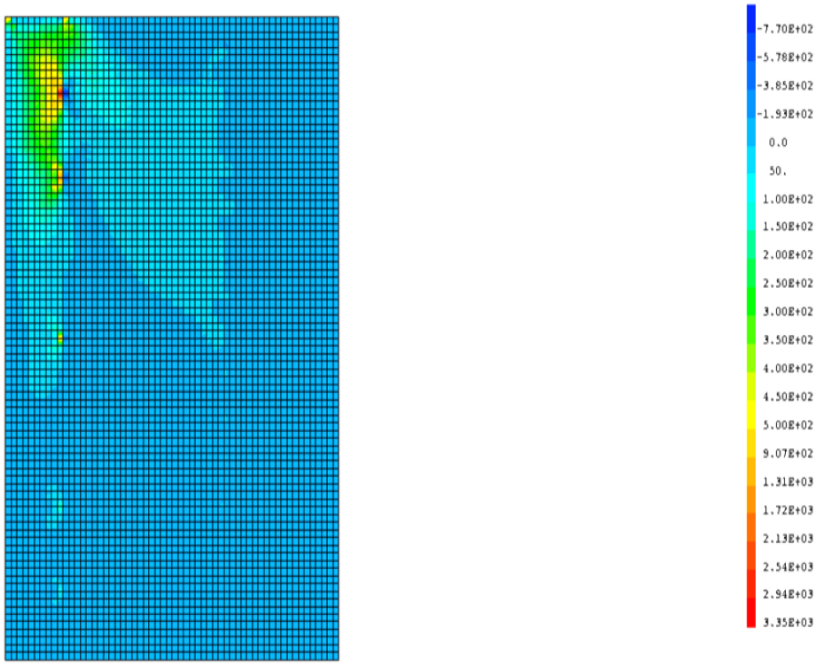

Figure 9: *Local shear stress snapshot of the small non-confined wall under shear loading conditions at failure for an identified ultimate crack length* $l_u = 1.51\ \mu m$

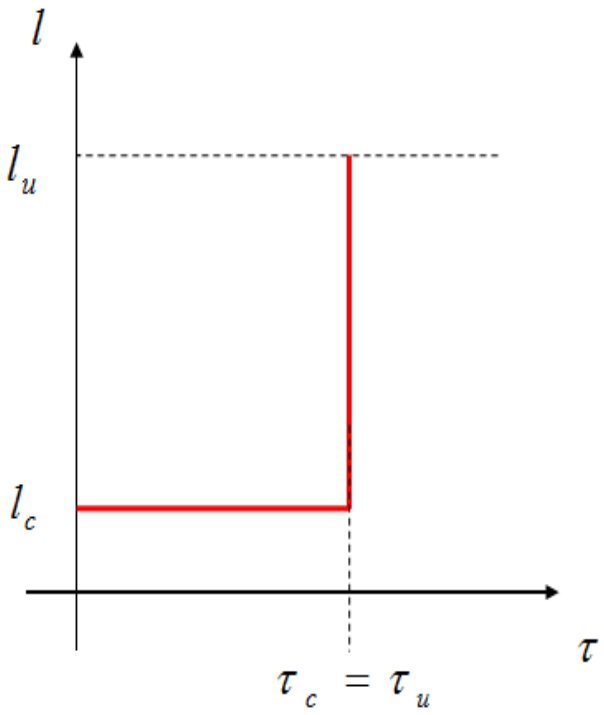

Figure 10: *A pre-assumed function describing the evolution of the crack half length with respect to the shear stress applied: the case of a diagonal compressed wall (with and without a unilateral contact condition).*

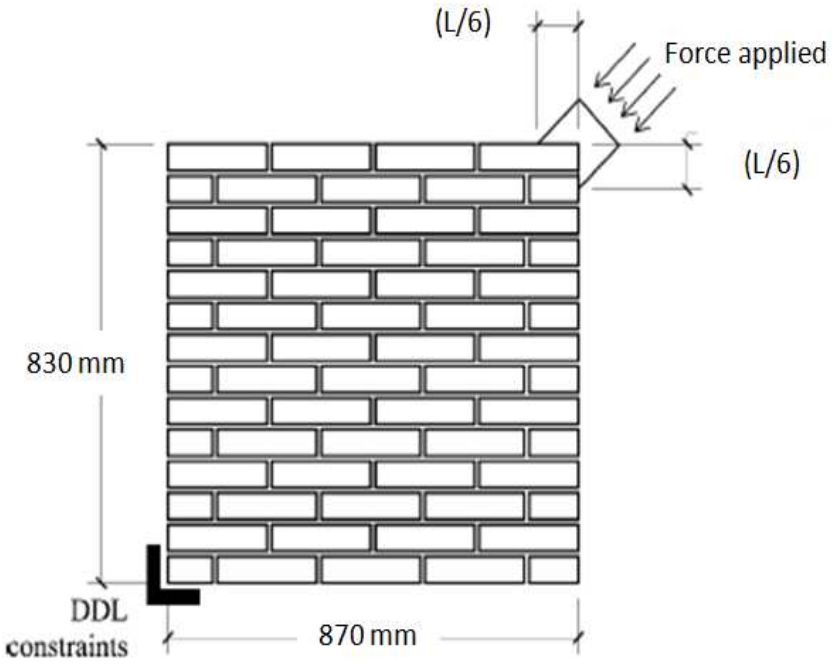

Figure 11: *Initial geometrical configuration and loading conditions imposed on the wall.*

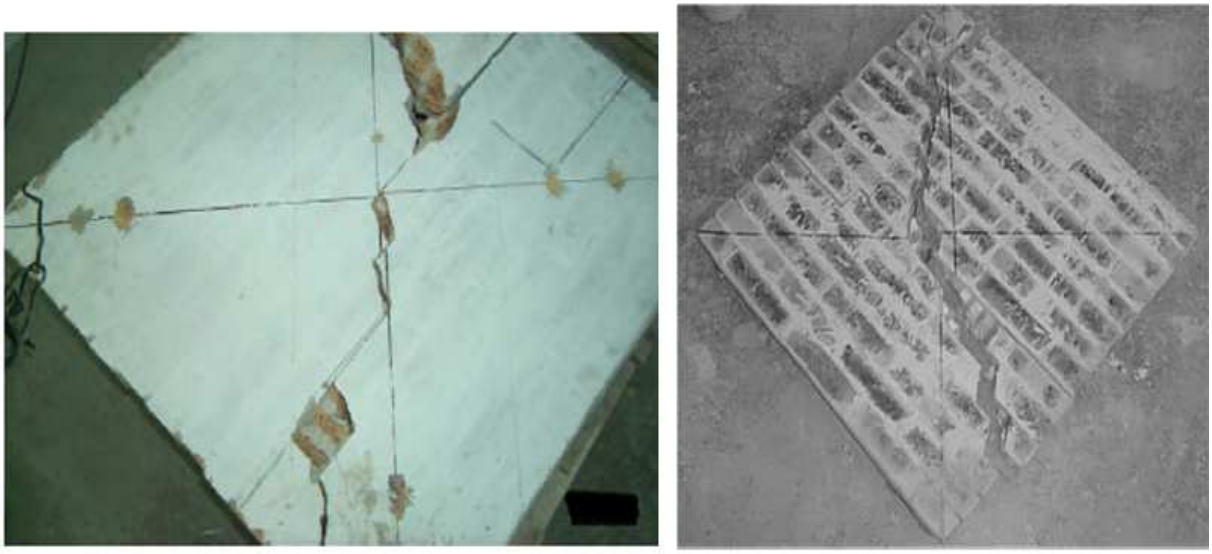

Figure 12: *Deformation of a wall subjected to diagonal compression: experimental tests from [33].*

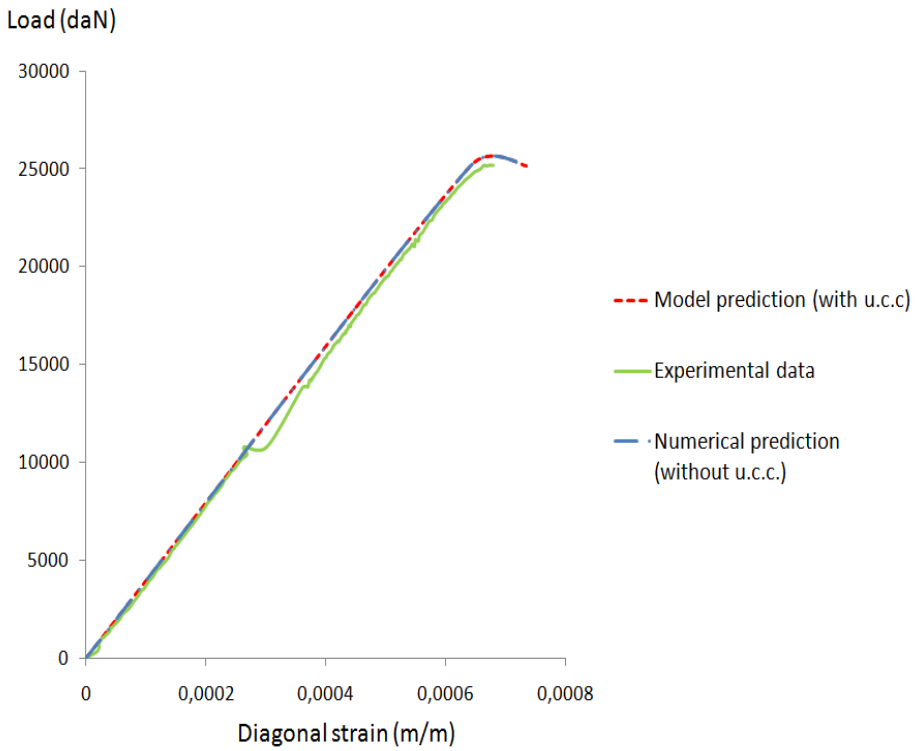

Figure 13: *"Stress-diagonal strain" diagrams of the wall (with and without a unilateral contact condition) under diagonal compression loading conditions: numerical and experimental results.*

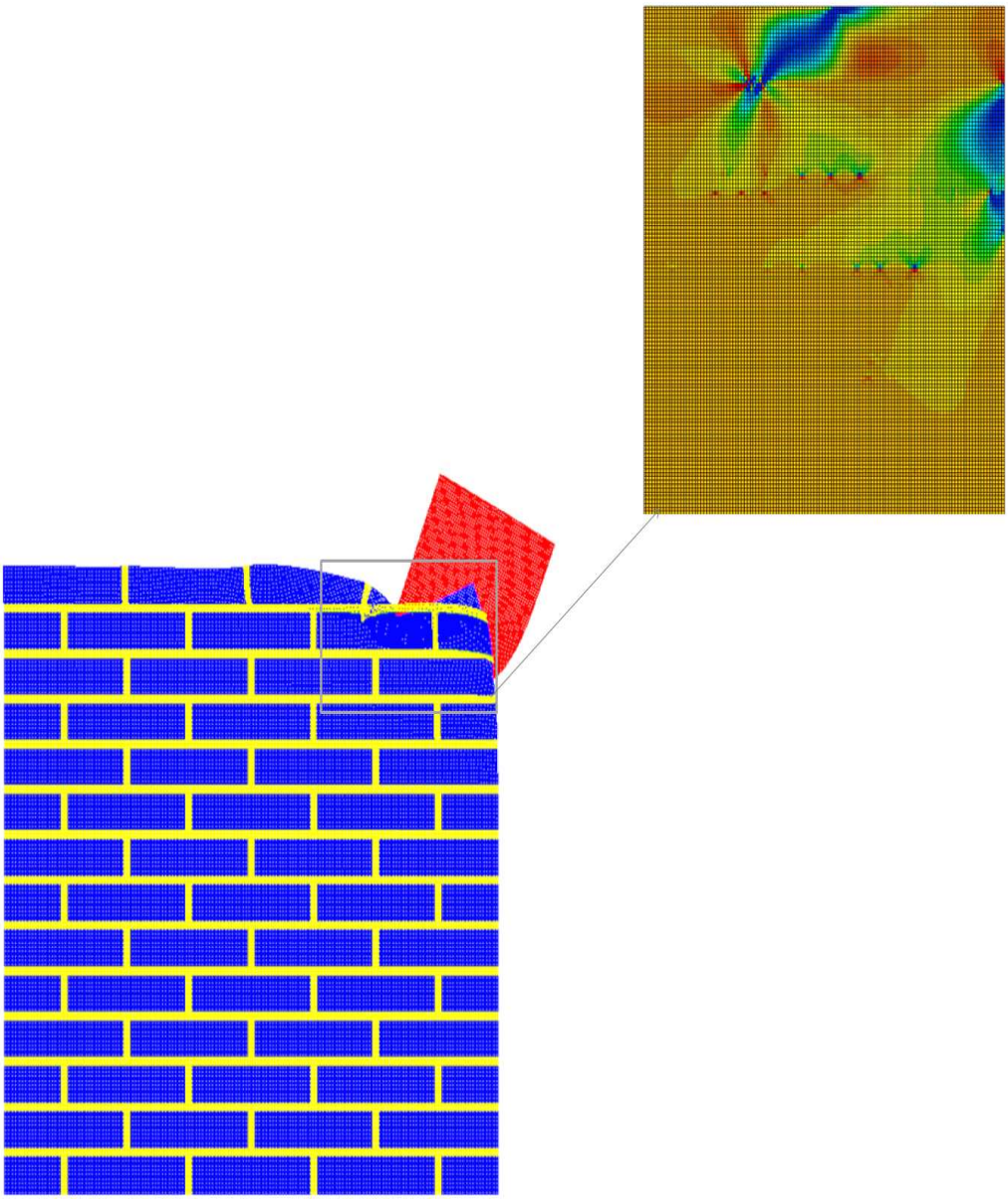

Figure 14: *Deformation and local shear stress snapshot at the corner of a wall (without the unilateral contact condition) subjected to diagonal compression: numerical test with the identified ultimate crack length value* $l_u = 1.61\ \mu m$.

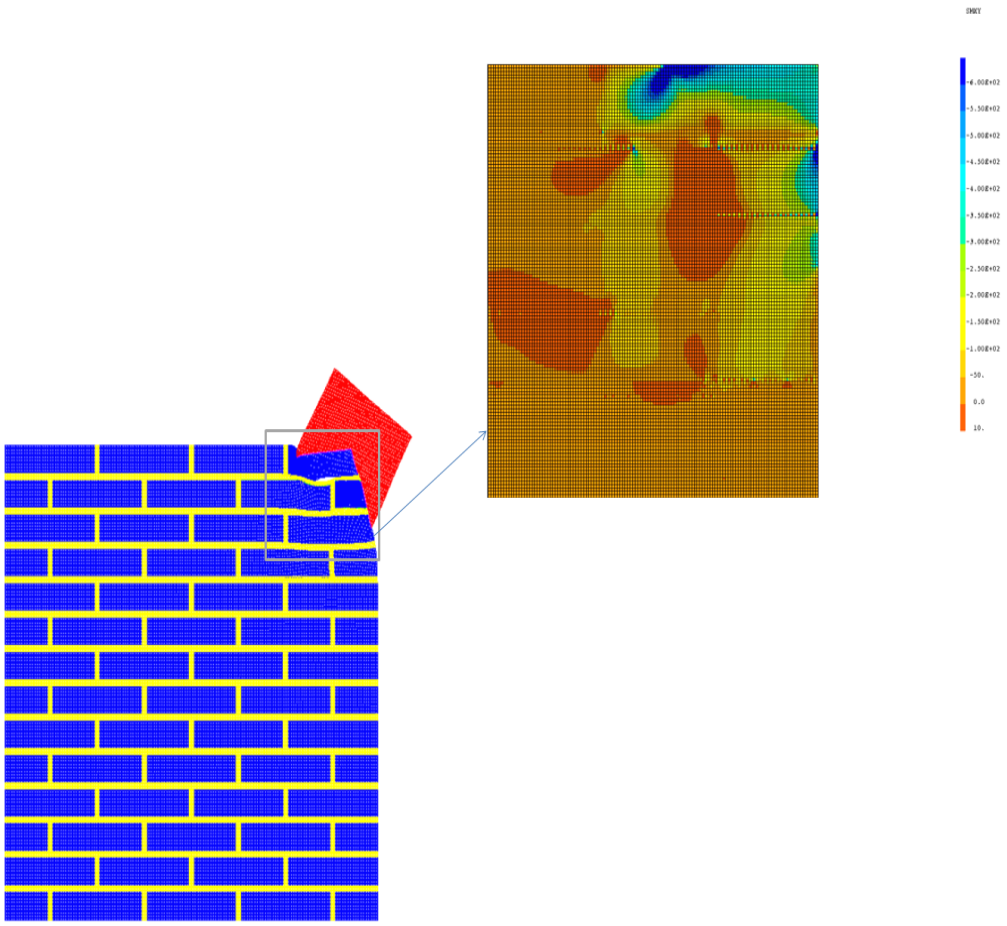

Figure 15: *Effect of the additional unilateral contact condition: Deformation and local shear stress snapshot at the corner of a wall subjected to diagonal compression. Numerical test with the identified ultimate crack length value* $l_u = 1.728\ \mu m$

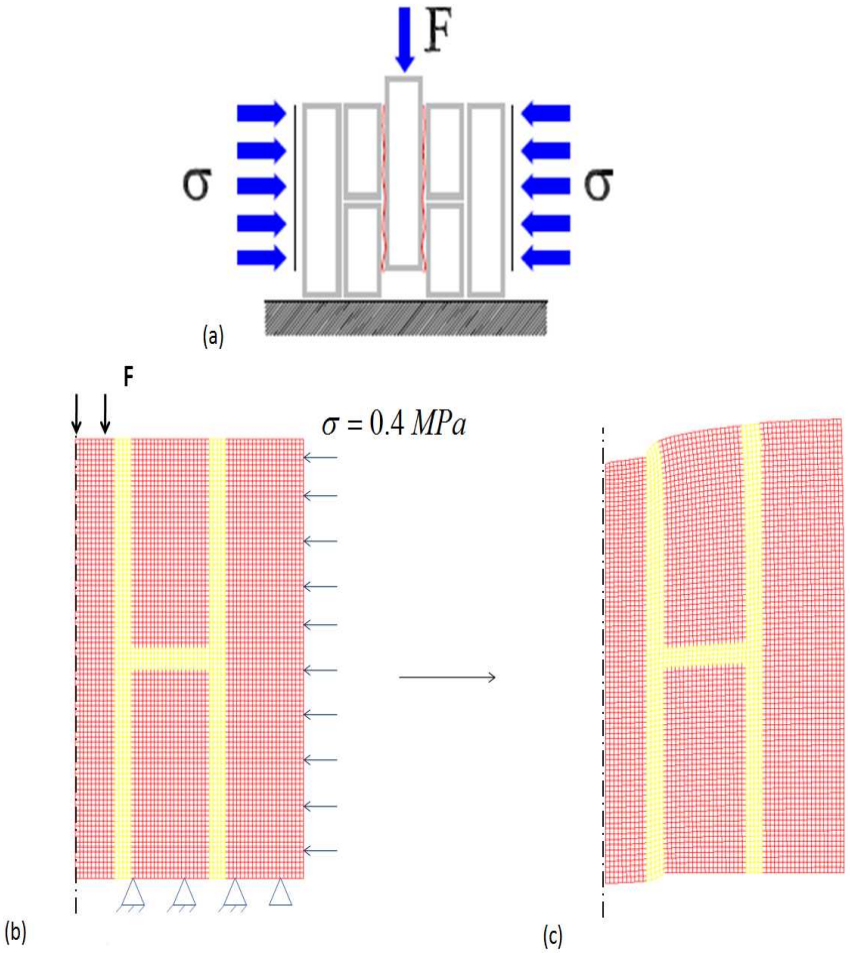

Figure 16: *Initial geometrical configuration and loading conditions imposed on a small confined wall (a, b), deformation of the small wall in a shear test (c)*

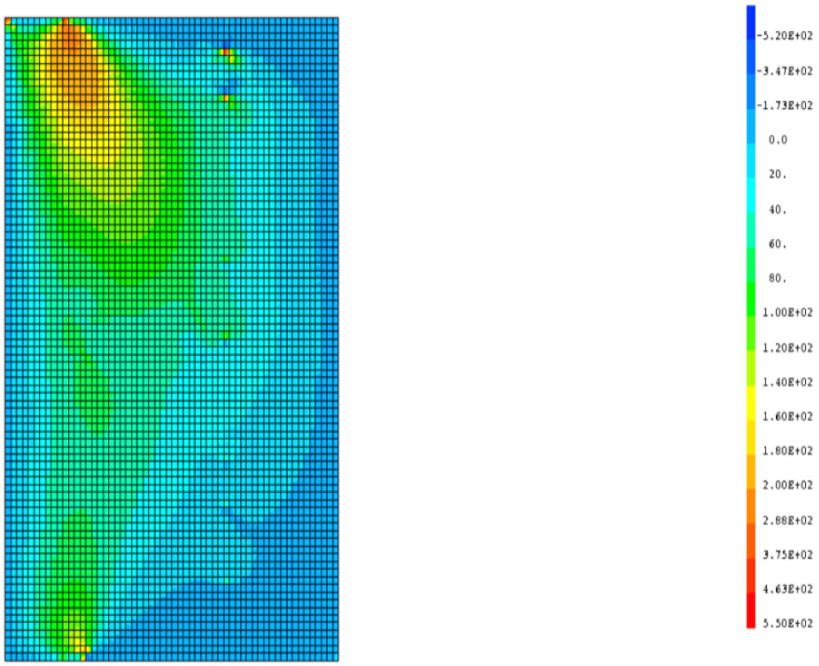

Figure 17: *Local shear stress snapshot of a confined small wall ($\sigma = 0.4\,MPa$) under shear loading conditions at failure (the identified ultimate crack length is $l = 1.57\,\mu m$)*

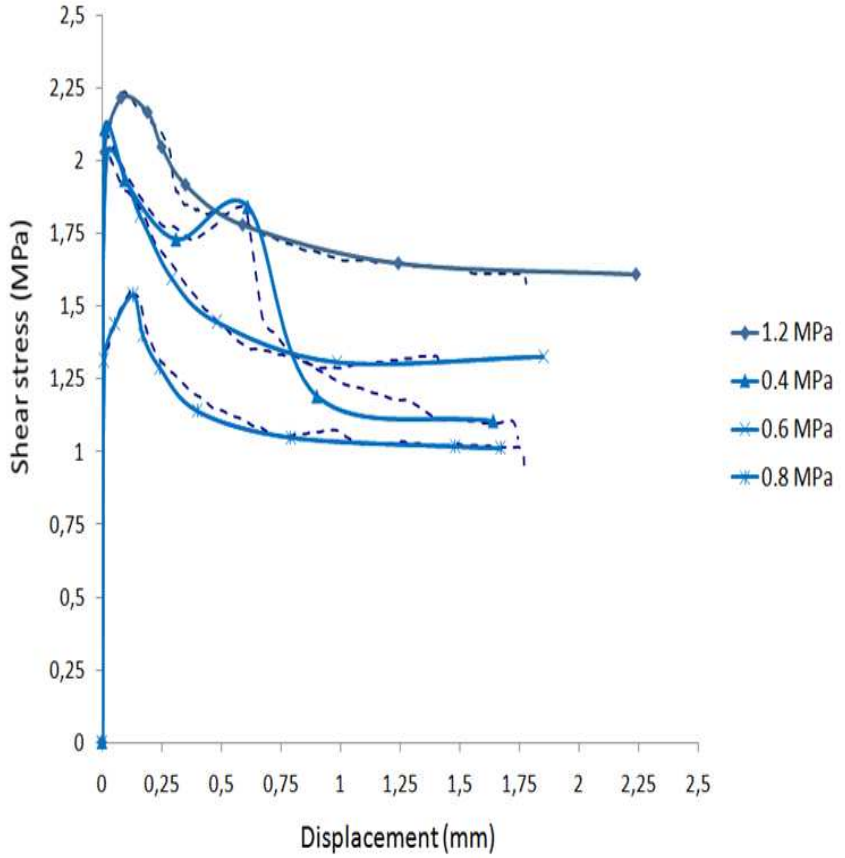

Figure 18: *Effect of the confining pressure: Experimental and numerical "shear stress-displacement" diagrams of a small confined wall under shear loading conditions.*

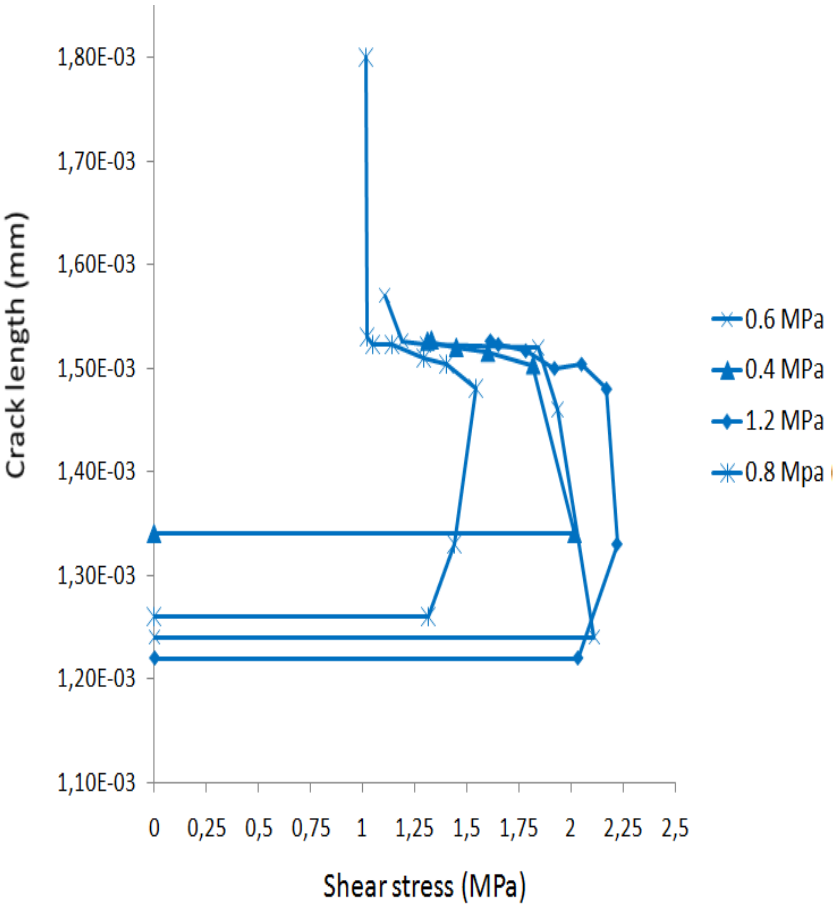

Figure 19: *Identified crack length laws giving the best fit between experimental and numerical data on confined small walls under shear loads and various confining pressures*

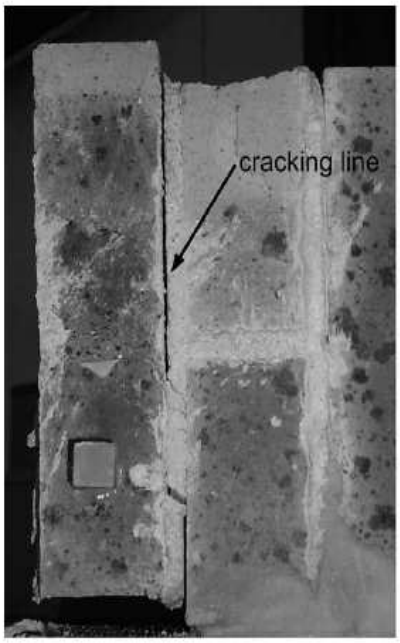

Figure 20: *Experimental deformation of a small confined wall under shear loading conditions [34]*

List of Tables

Young's modulus (MPa) of full brick	12800
Poisson's ratio of full brick	0.2
Young's modulus (MPa) of mortar	4000
Poisson's ratio of mortar	0.2

Table 1: Mechanical properties of the prism and wall masonry constituents [33, 34]

confining stress σ (MPa)	l_u (μm)	$e_r(l_u)$ (%)
0.4	1.57	2.5
0.6	1.53	5
0.8	1.8	11.1
1.2	1.53	5

Table 2: Identified ultimate representative crack length and the corresponding relative errors obtained on small confined walls under shear loading and different confining pressures

unilateral contact condition	l_u (μm)	$e_r(l_u)$ (%)
with	1.61	3
without	1.728	4

Table 3: Identified ultimate representative crack length and the corresponding relative errors obtained on a diagonally compressed wall with and without a unilateral contact condition

	l_u or average of l_u (μm)	$e_r(l_u)$ (%)	$e_r(C_N)$ (%)
non-confined prism	1.51	5.8	+ 17.4
confined prism	1.61	0.6	-2
wall (with/without u.c.c.)	1.66	3.7	-11

Table 4: Relative errors in the identified (average) ultimate representative crack lengths and stiffnesses in the case of masonries of various sizes under shear loading or diagonal compression conditions